



HAL
open science

Computation and characterization of local sub-filter-scale energy transfers in atmospheric flows

Davide Faranda, Valerio Lembo, Denis Kuzzay, Francois Daviaud, Berengere
Dubrulle

► **To cite this version:**

Davide Faranda, Valerio Lembo, Denis Kuzzay, Francois Daviaud, Berengere Dubrulle. Computation and characterization of local sub-filter-scale energy transfers in atmospheric flows. 2017. hal-01566028v1

HAL Id: hal-01566028

<https://hal.science/hal-01566028v1>

Preprint submitted on 20 Jul 2017 (v1), last revised 15 Mar 2018 (v3)

HAL is a multi-disciplinary open access archive for the deposit and dissemination of scientific research documents, whether they are published or not. The documents may come from teaching and research institutions in France or abroad, or from public or private research centers.

L'archive ouverte pluridisciplinaire **HAL**, est destinée au dépôt et à la diffusion de documents scientifiques de niveau recherche, publiés ou non, émanant des établissements d'enseignement et de recherche français ou étrangers, des laboratoires publics ou privés.

1 **Computation and characterization of local sub-filter-scale energy transfers**
2 **in atmospheric flows**

3 Davide Faranda^{1*}, Valerio Lembo², Denis Kuzzay³,
4 Francois Daviaud⁴ & Berengere Dubrulle⁴,

5 ¹*Laboratoire des Sciences du Climat et de l'Environnement, LSCE/IPSL, CEA-CNRS-UVSQ,*
6 *Université Paris-Saclay, F-91191 Gif-sur-Yvette, France*

7 *davide.faranda@lsce.ipsl.fr*

8 ²*Meteorological Institute, University of Hamburg, Grindelberg 5, 20146 Hamburg, Germany*

9 ³*Univ Lyon, Ens de Lyon, Univ Claude Bernard, CNRS, Laboratoire de Physique, F-69342 Lyon,*
10 *France*

11 ⁴*SPEC, CEA, CNRS, Université Paris-Saclay, CEA Saclay 91191 Gif sur Yvette cedex, France*

12 **Corresponding author address: Laboratoire de Sciences du Climat et de l'Environnement, UMR*
13 *8212 CEA-CNRS-UVSQ,IPSL, Université Paris-Saclay, 91191 Gif-sur-Yvette, France.*

ABSTRACT

15 Atmospheric motions are governed by turbulent motions associated to non-
16 trivial energy transfers at small scales (direct cascade) and/or at large scales
17 (inverse cascade). Although it is known that the two cascades coexist, energy
18 fluxes have been previously investigated from the spectral point of view but
19 not on their instantaneous spatial and local structure. Here, we compute local
20 and instantaneous sub-filter scale energy transfers in two sets of reanalyses
21 (NCEP-NCAR and ERA-Interim) in the troposphere and the lower strato-
22 sphere for the year 2005. The fluxes are mostly positive (towards subgrid
23 scales) in the troposphere and negative in the stratosphere reflecting the baro-
24 clinic and barotropic nature of the motions respectively. The most intense
25 positive energy fluxes are found in the troposphere and are associated with
26 baroclinic eddies or tropical cyclones. The computation of such fluxes can be
27 used to characterize the amount of energy lost or missing at the smallest scale
28 in climate and weather models.

29 **1. Introduction**

30 Large scale atmospheric motions are modeled via a set of nonlinear equations known as primi-
31 tive equations (Smagorinsky 1963). They include an equation for mass conservation, the thermal
32 energy equation and the evolution equations of velocity fields. The latter are derived from the
33 Navier-Stokes equations on spherical geometry under the hydrostatic assumption, i.e. that vertical
34 motion is much smaller than horizontal motion. Such equations are the cornerstone of all weather
35 and climate models and their explicit implementation depends on the choice of coordinate system
36 and the resolution of the model (Cao and Titi 2007; Klein 2010; Stevens and Bony 2013; Cao et al.
37 2015). In the classical turbulence phenomenology, valid for isotropic and homogeneous flows, en-
38 ergy is injected at large scales, transferred downscale at a constant averaged rate ε (Kolmogorov
39 (1941) cascade) and dissipated at small scales by viscous effects (Frisch 1995). Due to rotation and
40 inertial effects, atmospheric flows are rotating and stratified (Holton and Hakim 2012). Turbulence
41 in such condition is known to develop a complex dynamics, as revealed by accurate numerical sim-
42 ulations and laboratory experiments (Levich and Tzvetkov 1985; Schertzer et al. 1997; Falkovich
43 1992; Pouquet and Marino 2013). Depending on the scale of the flow, energy transfers can be
44 directed either towards smaller scales (direct cascade) or towards larger scales (inverse cascade)
45 (Bartello 1995).

46 To date, there is no general consensus about the existence of dual cascades in atmospheric mo-
47 tions. Observed energy spectra in the troposphere and in the lower stratosphere (Nastrom and
48 Gage 1985) exhibit $k^{-5/3}$ law, generally connected to direct cascades, and/or k^{-3} power laws,
49 associated to an inverse energy cascade. The inverse cascade has been historically associated to
50 the quasi-geostrophic two dimensional dynamics induced by rotation (Charney 1971), and fed by
51 baroclinic instability. Tung and Orlando (2003) simulated the Nastrom-Gage energy spectrum of

52 atmospheric turbulence as a function of wavelength with a two-level quasigeostrophic model, and
53 were able to obtain both spectral behaviors with this simple dynamics. Kitamura and Matsuda
54 (2006) analyzed the role of stratification and rotation in the generation of the cascades, observing
55 that in experiments without planetary rotation, the obtained spectral slope was steeper and energy
56 transfer to larger vertical wave-numbers was increased. Some theories for a mesoscale inverse
57 cascade for stratified (not quasi-geostrophic) turbulence were proposed by Gage (1979) and Lilly
58 (1983) but these are no longer considered viable. According to Lindborg (2005), atmospheric
59 mesoscale $-5/3$ energy spectra can be explained by the existence of a direct cascade arising in the
60 limit of strong stratification while the role of planetary rotation is to inhibit the cascade process
61 at large scales leading to an accumulation of kinetic energy and steepening of the kinetic energy
62 spectrum at small wave numbers. Evidence on the existence of a direct energy cascade comes from
63 high resolution direct numerical simulations of stratified flows (Lindborg 2006). They also sug-
64 gest that the direction of the cascade may be crucially dependent on the ratio of the Brunt-Vaissala
65 frequency to the rotation frequency.

66 A way to clarify the situation is to compute the energy fluxes. In the classical picture of turbu-
67 lence, such energy transfers are related to the skewness of the distribution of velocity increments,
68 and the direction of the cascade is provided by the sign of the skewness (positive for direct cas-
69 cade, negative for inverse cascade). This quantity has thus been used in the past to quantify the
70 direction of the energy transfer. From the observed stratospheric third-order structure function,
71 Lindborg and Cho (2001) argued that there is a forward energy cascade in the mesoscale range of
72 atmospheric motions. In that study the authors pointed out that for scale smaller than 100 km the
73 statistical inhomogeneities can be neglected while this assumption is not valid for larger scales.
74 Similar conclusions also hold for the study of intense phenomena such as in tropical cyclones

75 (Tang and Chan 2015) and suggests that one must be careful in using skewness based approaches
76 to infer energy fluxes depending on the homogeneity assumptions.

77 Another approach to compute energy fluxes for atmospheric model is to rely on the spectral
78 kinetic energy budgets (see e.g. Augier and Lindborg (2013) and Peng et al. (2015) . However,
79 like the skewness approach, these computations only provide a global in space estimate of the
80 energy transfers and not their local value, nor their instantaneous spatial distribution.

81 An important breakthrough was made when Duchon and Robert (2000) reformulated the notion
82 of local energy budget using a weak formulation of the Navier-Stokes equations, allowing for
83 the definition of energy transfers local in space and time. It is valid for any geometry including
84 when strong inhomogeneity and anisotropy is present. Its ability to provide interesting information
85 about energy transfers at a given scale ℓ has been so far exploited in the experimental set-up of
86 the Von Karman swirling flow to measure the inertial energy transfers (Kuzzay et al. 2015; Saw
87 et al. 2016). The Duchon and Robert indicator requires only the 3D velocity fields and provides,
88 for each instant, 3D maps of the inertial sub-grid energy transfers at a scale ℓ . The interest of this
89 formulation is that it is devoid of any adjustable parameters unlike, for exemple, local estimates of
90 energy budgets based on LES methods Kuzzay et al. (2015).

91 In this work we adapt the definition of such indicators to the atmospheric dynamics providing
92 the first local maps of sub-filter-scale energy transfers without any adjustable parameter. The goal
93 of this work is i) to identify and characterize the atmospheric motions responsible for large energy
94 transfers and ii) to compute global time and spatial average and assess whether the reanalyses
95 over(under)-represent energy fluxes. The paper is structured as follows. After presenting the
96 indicator, we will study these transfers in the NCEP-NCAR and ERA-Interim reanalyses - to
97 ensure that results are model independent - for the year 2005 and investigate: i) the vertical and
98 horizontal global averages, ii) the distribution of energy transfers at different scales, iii) two case

99 studies of intense cyclones that occurred in 2005 (Katrina and Jolina) and also correspond to
 100 extreme energy transfers according to our indicator. We finally discuss the implications of our
 101 results on a theoretical and practical level.

102 2. Methods

103 Duchon and Robert (2000) defined energy transfers in a fluid at an arbitrary scale ℓ using a
 104 local energy balance equation based on the weak solution formalism of Leray (1934) and on the
 105 ideas of Onsager (1949). For this, they consider a sequence of coarse-grained solutions of the
 106 Navier-Stokes equations at a scale ℓ :

$$\begin{cases} \partial_t u_i^\ell + u_j^\ell \partial_j u_i^\ell = -\partial_j \tau^{ij} - \partial_i P^\ell + \nu \partial_j \partial_j u_i^\ell & (1) \\ \partial_j u_j^\ell = 0. & (2) \end{cases}$$

107 where u_i are the components of the velocity field and P the pressure, and derive the correspond-
 108 ing energy balance:

$$\partial_t E^\ell + \partial_j \left(u_j (E^\ell + P^\ell) - \nu \partial_j E^\ell \right) = -\nu \partial_j u_i^\ell \partial_j u_i^\ell - \mathcal{D}_\ell, \quad (3)$$

109 where $E^\ell = \frac{u_i^\ell u_i^\ell}{2}$ is the kinetic energy per unit mass at scale ℓ , \mathcal{D}_ℓ is expressed in terms of velocity
 110 increments $\delta \vec{u}(\vec{r}, \vec{x}) \stackrel{def}{=} \vec{u}(\vec{x} + \vec{r}) - \vec{u}(\vec{x}) \equiv \delta \vec{u}(\vec{r})$ (the dependence on ℓ and \vec{x} is kept implicit) as:

$$\mathcal{D}_\ell(\vec{u}) = \frac{1}{4\ell} \int_{\mathcal{V}} d\vec{r} (\vec{\nabla} G_\ell)(\vec{r}) \cdot \delta \vec{u}(\vec{r}) |\delta \vec{u}(\vec{r})|^2, \quad (4)$$

111 where G is a smooth filtering function, non-negative, spatially localized and such that
 112 $\int d\vec{r} G(\vec{r}) = 1$. The function G_ℓ is rescaled with ℓ as $G_\ell(\vec{r}) = \ell^{-3} G(\vec{r}/\ell)$. As noticed by Duchon
 113 and Robert, the average of $\mathcal{D}_\ell(\vec{u})$ ¹ coincides exactly with the statistical mean rate of inertial energy

¹we will refer also to it as “the DR indicator”

114 dissipated per unit mass as it can be derived from the anisotropic version of the Karman-Howarth
115 equation (Frisch 1995). The importance of their work relies on the fact that it provides a local non-
116 random form of the Karman-Howarth-Monin equation (Eyink 2002), valid even for anisotropic,
117 inhomogeneous flows as those associated with the atmospheric motions. The sign of $\mathcal{D}_\ell(\vec{u})$ pro-
118 vides the direction of the fluxes in the scale space: a positive sign implies transfer towards the
119 scales smaller than ℓ . Kuzzay et al. (2015) have shown the validity of the indicator in the case of a
120 turbulent axisymmetric von Kármán flow where the contribution of $\mathcal{D}_\ell(\vec{u})$ over the whole volume
121 of the experiment agrees with global direct torque measurements of the injected power within 2%
122 at large Reynolds numbers, as long as the scale ℓ lies in the inertial range .

123 Note that it is possible to implement the expression of $\mathcal{D}_\ell(\vec{u})$ in climate models as it demands
124 only the numerical 3D velocity fields. Moreover, the intrinsic structure of $\mathcal{D}_\ell(\vec{u})$ makes it less
125 sensitive to noise than classical gradients, or even than the usual Kármán-Howarth relation: in-
126 deed, the derivative in scale is not applied directly to the velocity increments, but rather on the
127 smoothing function, followed by a local angle averaging. This guarantees that no additional noise
128 is introduced by the procedure. Even more, the noise coming from the estimate of the velocity is
129 naturally averaged out by the angle smoothing as shown in Kuzzay et al. (2015). In the same study,
130 the authors argued that the Duchon and Robert approach was a better alternative to the widespread
131 large eddies simulation based method for the computation of energy fluxes, since it relies on very
132 few arbitrary hypotheses. Experimentally, in the von Karman set-up, the DR formula provided a
133 better estimate of the energy dissipation than the LES method : in particular, estimates of the in-
134 jected and dissipated powers were within 20% of the measured value using the LES-PIV method,
135 whereas reached 98% of the actual dissipation rate of energy with the DR formula Kuzzay et al.
136 (2015).

137 We have investigated the occurrence of high and low values of $\mathcal{D}_\ell(\vec{u})$ in the von Kármán swirling
138 flow and identified some typical shape of the velocity field structures corresponding to those val-
139 ues. In general, positive values of $\mathcal{D}_\ell(\vec{u})$ are measured whenever there is a strong convergence
140 of the flow. These dissipative structures are represented in Figure 1 and can be associated with a
141 front, a jet or a vortex. The corresponding divergent flows are instead associated to negative values
142 of $\mathcal{D}_\ell(\vec{u})$, and they point to injection of energy from the sub-grid scales. As we will see in Section
143 3.1 for real atmospheric flows, dipolar $\mathcal{D}_\ell(\vec{u})$ structures may appear with 3D structures as those
144 observed during hurricanes.

145 3. Analysis

146 For this study, outputs of the ERA-Interim and NCEP-NCAR Reanalysis 1 have been
147 used. ERA-Interim is the currently operational Reanalysis product at the European Center for
148 Medium-Range Weather Forecasting (ECMWF) (Dee et al. 2011). Released in 2007, it provides
149 reanalyzed data from 1979 to nowadays, stored at an original T255 spectral resolution (about
150 80 km horizontal resolution), with 60 vertical hybrid model levels. A 12h four-dimensional
151 variational data assimilation (4D-Var) is adopted. As a forecast model, the Integrated Forecast
152 Model (IFS), Cy31r2 release, is used, fully coupling modules for the atmosphere, ocean waves
153 and land surface. Sea-surface temperatures (SST) and sea-ice concentration (SIC) are ingested
154 as boundary conditions and interpolated on a reduced-Gaussian grid as needed. In our case
155 zonal, meridional and vertical wind components are considered at a $0.75^\circ \times 0.75^\circ$ horizontal
156 resolution over 12 pressure levels between 1000 and 100 hPa. A 12h time-step is considered.
157 Known problems concerning these datasets are the lack of dry mass conservation (Berrisford et al.
158 2011) and the slight asymmetry between evaporation and precipitation (Dee et al. 2011). The
159 turbulent fluxes are based on the tiled ECMWF scheme for surface exchanges over land (Viterbo

160 and Beljaars 1995; Viterbo and Betts 1999). Each gridbox is divided into up to six fractions
161 (over land) depending on the type of surface, having different transfer coefficients based on a
162 Monin-Obukhov formulation. Similarly, over oceans, two different coefficients are used for stable
163 and unstable conditions (Beljaars 1995).

164
165 NCEP-NCAR Reanalysis 1 has been developed in a joint effort by the National Center for Envi-
166 ronmental Prediction (NCEP) and the National Center for Atmospheric Research (NCAR) (Kalnay
167 et al. 1996). The simulation is operational since January 1995, covering a period from 1948 to
168 nowadays. Data assimilation is performed via a 3D variational scheme (Parrish and Derber 1992).
169 The NCEP model system, operational in 1994, has been used for forecasting. It features a T62
170 spectral resolution, corresponding to a $2.5^\circ \times 2.5^\circ$ horizontal grid (about 200 km horizontal reso-
171 lution), with 28 sigma levels. Most of the major physical processes involving the climate system
172 are parametrized. SST, SIC, snow cover, albedo, soil wetness and roughness length are ingested as
173 boundary conditions. Data are archived at an original 6h time-step, and such a temporal resolution
174 is retained for our analysis. The atmospheric model which provides the NCEP/NCAR reanalysis
175 data, uses bulk aerodynamic formulas to estimate the turbulent fluxes, with exchange coefficients
176 depending on empirical profiles extending the Monin-Obukhov similarity relationship (Miyakoda
177 and Sirutis 1986). For more details on the comparison between different subgrid parametrization
178 of surface fluxes, one might refer to Brunke et al. (2011).

179 *a. Yearly and seasonal average local energy transfers*

180 We begin the analysis by studying the latitudinal averages and the horizontal distributions of the
181 DR indicator. In Figure 2 we show the results obtained for the ERA-Interim reanalysis at $\ell = 220$
182 km, slightly larger than the horizontal resolution of the coarser reanalysis (NCEP-NCAR). The

183 results are consistent with those obtained for the NCEP-NCAR reanalysis reported in Figure 3.
 184 The left panels of Figure 2-3 show the yearly average, the central ones the winter (DJF) average
 185 and the right ones the summer (JJA) average of the DR indicator. $\mathcal{D}_\ell(\vec{u})$ is mostly positive in the
 186 troposphere, about zero at the tropopause and negative in the lower stratosphere. The behavior of
 187 $\mathcal{D}_\ell(\vec{u})$ is clearly associated to that of the jet stream, and the most intense patterns are observed
 188 in winter for the northern hemisphere and summer for the southern hemisphere. We can explain
 189 the sign of the DR indicator by invoking the relation between baroclinic and barotropic flows and
 190 direct and inverse cascades (Tung and Orlando 2003). The baroclinic motions responsible for the
 191 genesis and decay of extratropical cyclones are mostly associated to direct cascades and positive
 192 $\mathcal{D}_\ell(\vec{u})$ contributions. Our results are therefore consistent with those found by Peng et al. (2015)
 193 who also found upscale transfer in the lower stratosphere at outer mesoscale length scales. On the
 194 contrary, the essential barotropic motions governing the lower stratosphere atmospheric dynamics,
 195 are associated to an inverse energy cascade and to negative values of the DR indicator. The
 196 change of sign of the $\mathcal{D}_\ell(\vec{u})$ with height is evident when looking at the DR indicator distribution
 197 shown in the upper panels of Figure 5. Results from ERA-Interim are shown in the left panels,
 198 from NCEP-NCAR in the right panels. The shape of the distribution recalls the one observed in
 199 the turbulent von Kármán swirling flow (Saw et al. 2016). The global average is slightly positive,
 200 i.e. both the reanalyses suffer from a small energy imbalance corresponding to underrepresented
 201 fluxes towards scales smaller than ℓ . Long tail distributions correspond to large excursions
 202 towards large positive (in the troposphere) or negative (in the lower stratosphere) energy fluxes.
 203 Although there is agreement between the ERA interim and the NCEP-NCAR data, the latter
 204 shows fatter tails. This might be due either to the different resolution of the datasets and/or on the
 205 different physical parametrizations. It is therefore worth investigating the dependence of $\mathcal{D}_\ell(\vec{u})$
 206 on the scale ℓ . These results are reported in the lower panels of Figure 5. It is apparent how by

207 measuring $\mathcal{D}_\ell(\vec{u})$ at larger scales we get lighter tails. This means that the energy imbalance of the
208 reanalyses is reduced when we look at motions whose characteristic scales are larger.

209

210 We further compare the $\mathcal{D}_\ell(\vec{u})$ results with the spectra $E(\ell)$ obtained at each pressure level
211 for the horizontal velocity fields and reported in Figure 4. Indeed the scale $\ell = 220$ km lies at
212 the crossover between $-5/3$ and -3 spectra, depending on the height: the spectra support then
213 the results obtained with the Duchon and Robert indicator, namely the upscale transfers in the
214 stratosphere associated to the -3 part of the spectrum and the $-5/3$ downscale transfers in the
215 troposphere. The lower quality of the NCEP-NCAR spectra for smaller ℓ scales also justify our
216 choice to restrict the analysis at $\ell > 220$ Km. .

217

218 To understand the relation between baroclinic eddies and scale dependence we analyze the maps
219 of $\mathcal{D}_\ell(\vec{u})$ collected each 6 or 12h depending on the datasets. They are collected for NCEP-NCAR
220 in the supplementary video. As an example, we report in Figure 6 the analysis for January, 6th at
221 midnight, issued from ERA-Interim. Large positive and negative values of the DR indicator are
222 found as dipoles in baroclinic eddies. When increasing the scale ℓ of the analysis, the tails become
223 lighter as the local positive and negative contributions get averaged out. To investigate better the
224 role of baroclinic eddies in the development of large DR values, we analyze two tropical cyclones
225 (Katrina and Jolina) whose life-cycle ended up as extratropical storms.

226 *b. Local energy transfers during hurricanes*

227 Some aspects of DR indicator evolution in Katrina and Jolina (Nabi) tropical cyclones case
228 studies are shown in Figures 7,8 and 9. These extreme events have been well documented in
229 the literature (Wang and Oey 2008; Harr et al. 2008; Hsiao et al. 2009). Here we observe that

230 hurricanes correspond to large values of the DR indicator and are extremely localized in space and
231 time. To have a finer understanding of their dynamics, we focus on these events by computing
232 $\mathcal{D}_\ell(\vec{u})$ in proximity of the cyclonic structures and we use the dataset at higher resolution (ERA-
233 Interim). At every time step, the cyclone is tracked as the region bordered by sea-level pressure
234 (SLP) values lower than 1005 hPa (in the case of Katrina), lower than 1000hPa (in the case of
235 Jolina). The threshold difference is motivated by the presence of other low pressure structures
236 in the region corresponding to Jolina’s trajectory. As the cyclones follow their path, a transition
237 occurs from a condition characterized by the alternation of negative and positive DR values, to one
238 characterized by dominant positive values. This is particularly evident in the middle levels of the
239 troposphere (between 850 hPa and 250 hPa).

240 Some relevant differences are found, comparing the two cyclones. On one hand, $\mathcal{D}_\ell(\vec{u})$ decreases
241 as Katrina moves northward, and the patterns of DR at higher levels apparently lose their co-
242 variability with the surface structure of the cyclone. On the other hand, the DR indicator remains
243 large as Jolina moves northward, preserving its vertical coherence. Furthermore, the land-sea
244 contrasts seems to have a role in shaping the DR patterns at lower levels, with Jolina possibly
245 deriving its strength from its permanence over a sea surface, even at mid-latitudes. While Katrina
246 loses its energy source as cyclonic system as soon as it move northward in the continental areas,
247 Jolina develops into a powerful extra-tropical storm, as also noticeable looking at the SLP values
248 at the center of the system (Harr et al. 2008).

249 The DR evolution during the lifetime of the two systems suggests that this quantity may well
250 represent the different natures of a tropical cyclone (which is typically barotropic) and an extrat-
251 ropical cyclone (which is in turn baroclinic). Dominant positive $\mathcal{D}_\ell(\vec{u})$ values reflect an unresolved
252 energy transfer towards the smaller scales, that is coherent with the downscale enstrophy transfer
253 by means of eddy-eddy interaction in baroclinic eddies (Burgess et al. 2013). The jet stream,

254 which is sustained by the eddy-mean flow interactions over mid-latitudes, is indeed denoted by
255 large positive DR values (cfr. Figure 2), enforcing the hypothesis that the downscale enstrophy
256 transfer is associated with an upscale kinetic energy transfer (Held and Hoskins 1985; Straus and
257 Ditlevsen 1999). A dipole vertical structure emerges, as shown in Figure 2, with opposite sign
258 DR values in coincidence of the jet stream. This is consistent with previous findings from general
259 circulation models (Koshyk and Hamilton 2001) and higher resolution Reanalyses (Burgess et al.
260 2013), showing a decay of synoptic scale rotational kinetic energy and a downscale transfer of
261 divergent kinetic energy above the jet stream and in correspondence to the tropopause.

262 **4. Discussion**

263 Weather and climate models do not resolve the viscous scales, which for the atmospheric mo-
264 tions are order of 0.1 mm (Priestley 1959). Up to date, their resolution ranges from $\simeq 2$ km of
265 regional weather models to $\simeq 100$ km of global climate models. To correctly represent dissipation
266 effects at a scale ℓ , the turbulent cascade needs to be parametrized at each grid point depending
267 on the type of motion and the geographical constraints. Despite the importance of such energy
268 transfers, their distribution and their time and spatial behavior is known only partially through
269 field campaigns (Lübken 1997) or by global averages (Sellers 1969; Seinfeld and Pandis 2016).
270 This does not ensure a global coverage and does not tell the direction of the energy transfers in the
271 free troposphere. In this paper, we have used Duchon and Robert (2000) to compute and charac-
272 terize the distribution of instantaneous and local sub-grid energy transfers in the atmosphere using
273 3D velocity fields obtained in NCEP-NCAR and ERA-Interim reanalysis. Those energy transfers
274 are highly correlated with the baroclinic eddies occurring at mid-latitudes and with severe tropical
275 cyclones. Our computation of local energy transfer provides the direction of the local energy cas-
276 cade at a certain scale ℓ in physical space. At the grid resolution l , the value of $\mathcal{D}_\ell(\vec{u})$ is an exact

277 measure of the amount of energy *that must be transferred to subgrid scales* (positive DR contri-
278 butions) or *that must be injected from the subgrid scales* (negative contributions) to the scale ℓ of
279 the analysis. This information could be used to interactively adjust the energy fluxes to account
280 for the energy conservation laws in the atmosphere (Lucarini and Ragone 2011). We have also
281 observed that extreme events as tropical and extratropical storms are associated with large values
282 of $\mathcal{D}_\ell(\vec{u})$, even at the ground.

283 The quantity $\mathcal{D}_\ell(\vec{u})$ is also a measure of the flux of energy that can be exploited in wind turbines
284 (Miller et al. 2011, 2015). Although our analysis is performed for large scale general circulation
285 models, the Duchon and Robert (2000) formula can be applied to regional climate and weather
286 prediction models. At smaller scales, it will be extremely interesting to analyze the relation be-
287 tween $\mathcal{D}_\ell(\vec{u})$ and the genesis of extreme wind gusts or even tornadoes. At such scales, one could
288 investigate the distributions of $\mathcal{D}_\ell(\vec{u})$ to the instantaneous subgrid scales dissipation obtained by
289 field measurements (Higgins et al. 2003). It will also been worth to investigate whether adaptive
290 asymptotic methods, as those proposed by Klein et al. (2001) or the Lagrangian scale-dependant
291 models for the subgrid scales in Large Eddy Simulations (Bou-Zeid et al. 2004), afford better
292 energy balances, i.e. the spatial and temporal average of $\mathcal{D}_\ell(\vec{u})$ is closer to zero.

293 Acknowledgments

294 D. Faranda was supported by ERC grant No. 338965. DF thanks G. Messori and N. Vercauteren
295 for useful discussions and comments on the paper.

296 References

297 Augier, P., and E. Lindborg, 2013: A new formulation of the spectral energy budget of the at-
298 mosphere, with application to two high-resolution general circulation models. *Journal of the*

299 *Atmospheric Sciences*, **70** (7), 2293–2308.

300 Bartello, P., 1995: Geostrophic adjustment and inverse cascades in rotating stratified turbulence.
301 *Journal of the atmospheric sciences*, **52** (24), 4410–4428.

302 Beljaars, A., 1995: The parametrization of surface fluxes in large-scale models under free convec-
303 tion. *Quarterly Journal of the Royal Meteorological Society*, **121** (522), 255–270.

304 Berrisford, P., P. Kållberg, S. Kobayashi, D. Dee, S. Uppala, a. J. Simmons, P. Poli, and H. Sato,
305 2011: Atmospheric conservation properties in ERA-Interim. *Quarterly Journal of the Royal*
306 *Meteorological Society*, **137** (July), 1381–1399, doi:10.1002/qj.864.

307 Bou-Zeid, E., C. Meneveau, and M. B. Parlange, 2004: Large-eddy simulation of neutral atmo-
308 spheric boundary layer flow over heterogeneous surfaces: Blending height and effective surface
309 roughness. *Water Resources Research*, **40** (2).

310 Brunke, M. A., Z. Wang, X. Zeng, M. Bosilovich, and C.-L. Shie, 2011: An assessment of the
311 uncertainties in ocean surface turbulent fluxes in 11 reanalysis, satellite-derived, and combined
312 global datasets. *Journal of Climate*, **24** (21), 5469–5493.

313 Burgess, B. H., A. R. Erler, and T. G. Shepherd, 2013: The troposphere-to-stratosphere transition
314 in kinetic energy spectra and nonlinear spectral fluxes as seen in ecmwf analyses. *Journal of the*
315 *Atmospheric Sciences*, **70** (2), 669–687.

316 Cao, C., S. Ibrahim, K. Nakanishi, and E. S. Titi, 2015: Finite-time blowup for the inviscid primi-
317 tive equations of oceanic and atmospheric dynamics. *Communications in Mathematical Physics*,
318 **337** (2), 473–482.

319 Cao, C., and E. S. Titi, 2007: Global well-posedness of the three-dimensional viscous primitive
320 equations of large scale ocean and atmosphere dynamics. *Annals of Mathematics*, 245–267.

- 321 Charney, J. G., 1971: Geostrophic turbulence. *Journal of the Atmospheric Sciences*, **28 (6)**, 1087–
322 1095.
- 323 Dee, D. P., and Coauthors, 2011: The ERA-Interim reanalysis: configuration and performance of
324 the data assimilation system. *Quarterly Journal of the Royal Meteorological Society*, **137 (656)**,
325 553–597, doi:10.1002/qj.828, URL <http://doi.wiley.com/10.1002/qj.828>.
- 326 Duchon, J., and R. Robert, 2000: Inertial energy dissipation for weak solutions of incompressible
327 euler and navier-stokes equations. *Nonlinearity*, **13 (1)**, 249.
- 328 Eyink, G. L., 2002: Local 4/5-law and energy dissipation anomaly in turbulence. *Nonlinearity*,
329 **16 (1)**, 137.
- 330 Falkovich, G., 1992: Inverse cascade and wave condensate in mesoscale atmospheric turbulence.
331 *Physical review letters*, **69 (22)**, 3173.
- 332 Frisch, U., 1995: *Turbulence: the legacy of AN Kolmogorov*. Cambridge university press.
- 333 Gage, K., 1979: Evidence for $k^{-5/3}$ law inertial range in mesoscale two-dimensional turbulence.
334 *Journal of the Atmospheric Sciences*, **36 (10)**, 1950–1954.
- 335 Harr, P. A., D. Anwender, and S. C. Jones, 2008: Predictability associated with the downstream
336 impacts of the extratropical transition of tropical cyclones: Methodology and a case study of
337 typhoon nabi (2005). *Monthly Weather Review*, **136 (9)**, 3205–3225.
- 338 Held, I. M., and B. J. Hoskins, 1985: Large-scale eddies and the general circulation of the tropo-
339 sphere. *Advances in Geophysics*, **28**, 3–31.
- 340 Higgins, C. W., M. B. Parlange, and C. Meneveau, 2003: Alignment trends of velocity gradients
341 and subgrid-scale fluxes in the turbulent atmospheric boundary layer. *Boundary-Layer Meteoro-*
342 *logy*, **109 (1)**, 59–83.

343 Holton, J. R., and G. J. Hakim, 2012: *An introduction to dynamic meteorology*, Vol. 88. Academic
344 press.

345 Hsiao, L.-F., M. S. Peng, D.-S. Chen, K.-N. Huang, and T.-C. Yeh, 2009: Sensitivity of typhoon
346 track predictions in a regional prediction system to initial and lateral boundary conditions. *Jour-*
347 *nal of Applied Meteorology and Climatology*, **48 (9)**, 1913–1928.

348 Kalnay, E., and Coauthors, 1996: The NCEP/NCAR 40-year reanalysis project. *Bulletin of*
349 *the American Meteorological Society*, **77**, 437–471, doi:10.1175/1520-0477(1996)077<0437:
350 TNYRPP>2.0.CO;2.

351 Kitamura, Y., and Y. Matsuda, 2006: The kh- 3 and kh- 5/3 energy spectra in stratified turbulence.
352 *Geophysical research letters*, **33 (5)**.

353 Klein, R., 2010: Scale-dependent models for atmospheric flows. *Annual review of fluid mechanics*,
354 **42**, 249–274.

355 Klein, R., N. Botta, T. Schneider, C.-D. Munz, S. Roller, A. Meister, L. Hoffmann, and T. Sonar,
356 2001: Asymptotic adaptive methods for multi-scale problems in fluid mechanics. *Practical*
357 *Asymptotics*, Springer, 261–343.

358 Kolmogorov, A. N., 1941: Dissipation of energy in locally isotropic turbulence. *Dokl. Akad. Nauk*
359 *SSSR*, Vol. 32, 16–18.

360 Koshyk, J. N., and K. Hamilton, 2001: The horizontal kinetic energy spectrum and spectral bud-
361 get simulated by a high-resolution troposphere-stratosphere-mesosphere gcm. *Journal of the*
362 *atmospheric sciences*, **58 (4)**, 329–348.

363 Kuzzay, D., D. Faranda, and B. Dubrulle, 2015: Global vs local energy dissipation: The energy
364 cycle of the turbulent von kármán flow. *Physics of Fluids (1994-present)*, **27 (7)**, 075 105.

- 365 Leray, J., 1934: Sur le mouvement d'un liquide visqueux emplissant l'espace. *Acta mathematica*,
366 **63 (1)**, 193–248.
- 367 Levich, E., and E. Tzvetkov, 1985: Helical inverse cascade in three-dimensional turbulence as
368 a fundamental dominant mechanism in mesoscale atmospheric phenomena. *Physics reports*,
369 **128 (1)**, 1–37.
- 370 Lilly, D. K., 1983: Stratified turbulence and the mesoscale variability of the atmosphere. *Journal*
371 *of the Atmospheric Sciences*, **40 (3)**, 749–761.
- 372 Lindborg, E., 2005: The effect of rotation on the mesoscale energy cascade in the free atmosphere.
373 *Geophysical research letters*, **32 (1)**.
- 374 Lindborg, E., 2006: The energy cascade in a strongly stratified fluid. *Journal of Fluid Mechanics*,
375 **550**, 207–242.
- 376 Lindborg, E., and J. Y. Cho, 2001: Horizontal velocity structure functions in the upper troposphere
377 and lower stratosphere. ii- theoretical considerations. *Journal of geophysical research*, **106**, 10.
- 378 Lübken, F.-J., 1997: Seasonal variation of turbulent energy dissipation rates at high latitudes as
379 determined by in situ measurements of neutral density fluctuations. *Journal of Geophysical*
380 *Research: Atmospheres*, **102 (D12)**, 13 441–13 456.
- 381 Lucarini, V., and F. Ragone, 2011: Energetics of climate models: Net energy balance and merid-
382 ional enthalpy transport. *Reviews of Geophysics*, **49 (1)**.
- 383 Miller, L. M., N. A. Brunzell, D. B. Mechem, F. Gans, A. J. Monaghan, R. Vautard, D. W. Keith,
384 and A. Kleidon, 2015: Two methods for estimating limits to large-scale wind power generation.
385 *Proceedings of the National Academy of Sciences*, **112 (36)**, 11 169–11 174.

386 Miller, L. M., F. Gans, and A. Kleidon, 2011: Estimating maximum global land surface wind
387 power extractability and associated climatic consequences. *Earth Syst. Dynam*, **2** (1), 1–12.

388 Miyakoda, K., and J. Sirutis, 1986: Manual of the e-physics. Available from Geophysical Fluid
389 Dynamics Laboratory, Princeton University, PO Box, **308**.

390 Nastrom, G., and K. S. Gage, 1985: A climatology of atmospheric wavenumber spectra of wind
391 and temperature observed by commercial aircraft. *Journal of the atmospheric sciences*, **42** (9),
392 950–960.

393 Onsager, L., 1949: Statistical hydrodynamics. *Il Nuovo Cimento (1943-1954)*, **6**, 279–287.

394 Parrish, D. F., and J. C. Derber, 1992: The national meteorological center’s spectral
395 statistical-interpolation analysis system. *Monthly Weather Review*, **120** (8), 1747–1763,
396 doi:10.1175/1520-0493(1992)120<1747:TnMCSS>2.0.CO;2, URL [http://dx.doi.org/10.1175/
397 1520-0493\(1992\)120<1747:TnMCSS>2.0.CO;2](http://dx.doi.org/10.1175/1520-0493(1992)120<1747:TnMCSS>2.0.CO;2).

398 Peng, J., L. Zhang, and J. Guan, 2015: Applications of a moist nonhydrostatic formulation of
399 the spectral energy budget to baroclinic waves. part i: The lower-stratospheric energy spectra.
400 *Journal of the Atmospheric Sciences*, **72** (5), 2090–2108.

401 Pouquet, A., and R. Marino, 2013: Geophysical turbulence and the duality of the energy flow
402 across scales. *Physical review letters*, **111** (23), 234 501.

403 Priestley, C. H. B., 1959: *Turbulent transfer in the lower atmosphere*. University of Chicago Press
404 Chicago.

405 Saw, E.-W., D. Kuzzay, D. Faranda, A. Guittonneau, F. Daviaud, C. Wiertel-Gasquet, V. Padilla,
406 and B. Dubrulle, 2016: Experimental characterization of extreme events of inertial dissipation
407 in a turbulent swirling flow. *Nature Communications*, **7**, 12 466.

408 Schertzer, D., S. Lovejoy, F. Schmitt, Y. Chigirinskaya, and D. Marsan, 1997: Multifractal cascade
409 dynamics and turbulent intermittency. *Fractals*, **5** (03), 427–471.

410 Seinfeld, J. H., and S. N. Pandis, 2016: *Atmospheric chemistry and physics: from air pollution to*
411 *climate change*. John Wiley & Sons.

412 Sellers, W. D., 1969: A global climatic model based on the energy balance of the earth-atmosphere
413 system. *Journal of Applied Meteorology*, **8** (3), 392–400.

414 Smagorinsky, J., 1963: General circulation experiments with the primitive equations: I. the basic
415 experiment*. *Monthly weather review*, **91** (3), 99–164.

416 Stevens, B., and S. Bony, 2013: What are climate models missing? *Science*, **340** (6136), 1053–
417 1054.

418 Straus, D. M., and P. Ditlevsen, 1999: Two-dimensional turbulence properties of the ecmwf re-
419 analyses. *Tellus A*, **51** (5), 749–772, doi:10.1034/j.1600-0870.1996.00015.x, URL [http://dx.doi.](http://dx.doi.org/10.1034/j.1600-0870.1996.00015.x)
420 [org/10.1034/j.1600-0870.1996.00015.x](http://dx.doi.org/10.1034/j.1600-0870.1996.00015.x).

421 Tang, C. K., and J. C. Chan, 2015: Idealized simulations of the effect of local and remote to-
422 pographies on tropical cyclone tracks. *Quarterly Journal of the Royal Meteorological Society*,
423 **141** (691), 2045–2056.

424 Tung, K. K., and W. W. Orlando, 2003: The k^{-3} and $k^{-5/3}$ energy spectrum of atmospheric
425 turbulence: Quasigeostrophic two-level model simulation. *Journal of the atmospheric sciences*,
426 **60** (6), 824–835.

427 Viterbo, P., and A. C. Beljaars, 1995: An improved land surface parameterization scheme in the
428 ecmwf model and its validation. *Journal of Climate*, **8** (11), 2716–2748.

429 Viterbo, P., and A. K. Betts, 1999: Impact on ecmwf forecasts of changes to the albedo of the bo-
430 real forests in the presence of snow. *Journal of Geophysical Research: Atmospheres*, **104 (D22)**,
431 27 803–27 810.

432 Wang, D.-P., and L.-Y. Oey, 2008: Hindcast of waves and currents in hurricane katrina. *Bulletin of*
433 *the American Meteorological Society*, **89 (4)**, 487–495.

434 **LIST OF FIGURES**

435 **Fig. 1.** Schematic representation of velocity fields (arrows) possibly originating large positive (orange) or negative (blue) local energy transfers $\mathcal{D}_\ell(\vec{u})$ (color patches). 23

436

437 **Fig. 2.** Distribution of $\mathcal{D}_\ell(\vec{u})$ for $\ell = 220$ Km and the ERA-Interim reanalysis. The left panels show the all 2005 year average, the central the winter average, the right panels the summer averages. The maps show the average $\mathcal{D}_\ell(\vec{u})$ for three different fixed height: 1000 hPa, 500 hPa and 100hPa. 24

438

439

440

441 **Fig. 3.** Distribution of $\mathcal{D}_\ell(\vec{u})$ for $\ell = 220$ Km and the NCEP-NCAR reanalysis. The left panels show the all 2005 year average, the central the winter average, the right panels the summer averages. The maps show the average $\mathcal{D}_\ell(\vec{u})$ for three different fixed height: 1000 hPa, 500 hPa and 100hPa. 25

442

443

444

445 **Fig. 4.** Solid lines: spectra $E(\ell)$ computed, at each pressure level, for the horizontal velocity fields. Dotted lines: $-5/3$ and -3 slopes. Magenta vertical lines: $\ell = 220$ Km. Top: NCEP-NCAR reanalysis, Bottom: ERA Interim reanalysis. 26

446

447

448 **Fig. 5.** Empirical $\mathcal{D}_\ell(\vec{u})$ density functions for ERA-Interim (left) and NCEP-NCAR (right) and the year 2005. Upper panel show the dependence on the height for $\ell = 220$ km, lower panel that on the scale. 27

449

450

451 **Fig. 6.** Instantaneous values of $\mathcal{D}_\ell(\vec{u})$ for ERA-Interim computed for January, 6th at midnight, for $\ell = 220$ km. Black Isolines show the sea level pressure field in hPa. 28

452

453 **Fig. 7.** Katrina Analysis: Spatial average $\langle \mathcal{D}_\ell(\vec{u}) \rangle$ for the region with $p < 1000$ hPa in the regions shown in the maps, obtained by the ERA-Interim reanalysis, for $\ell = 220$ km. The time interval is 12h and the dates correspond to midday. The maps show $\mathcal{D}_\ell(\vec{u})$ for three different levels (1000,700 and 200 hPa) at the time corresponding to the black arrows. 29

454

455

456

457 **Fig. 8.** Jolina Analysis: Spatial average $\langle \mathcal{D}_\ell(\vec{u}) \rangle$ for the region with $p < 1005$ hPa in the regions shown in the maps, obtained by the ERA-Interim reanalysis, for $\ell = 220$ km . The time interval is 12h and the dates correspond to midday. The maps show $\mathcal{D}_\ell(\vec{u})$ for three different levels (1000,700 and 200 hPa) at the time corresponding to the black arrows. 30

458

459

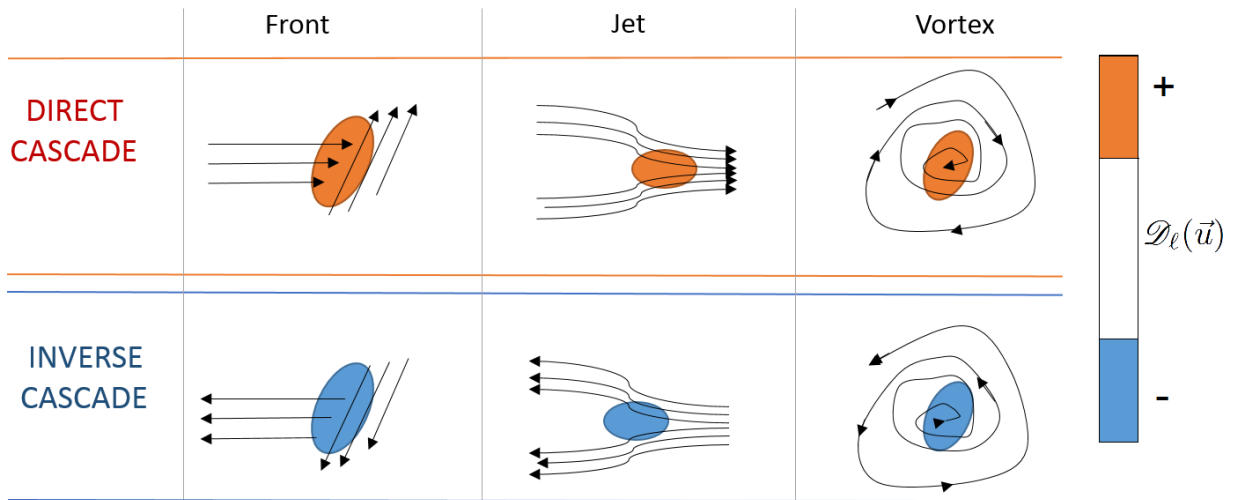
460

461 **Fig. 9.** 3D structure of the wind field (green cones) and $\mathcal{D}_\ell(\vec{u})$ for the Hurricane Katrina (top) and Jolina (bottom), obtained by the ERA-Interim reanalysis, for $\ell = 220$ km. Red: isosurfaces at $\mathcal{D}_\ell(\vec{u}) = 0.001$. Dark Blue: isosurfaces at $\mathcal{D}_\ell(\vec{u}) = -0.001$. The colorscale indicates values $\mathcal{D}_\ell(\vec{u}) > 0.001$. See supplementary videos for the animations. 31

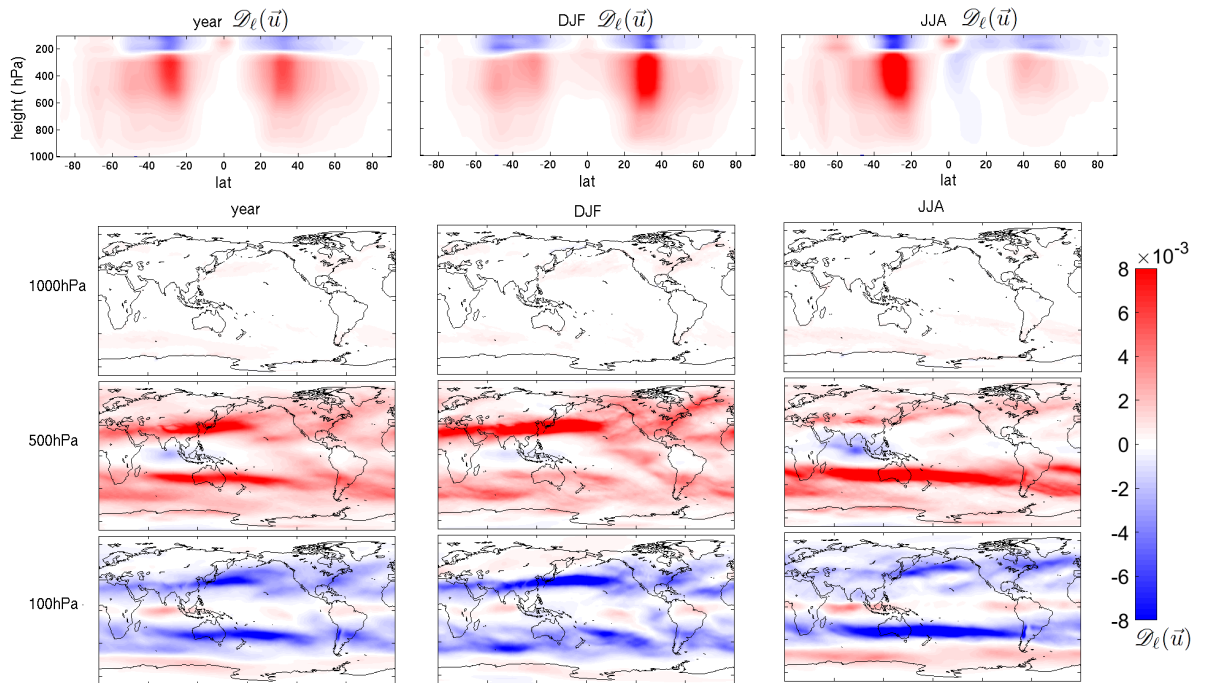
462

463

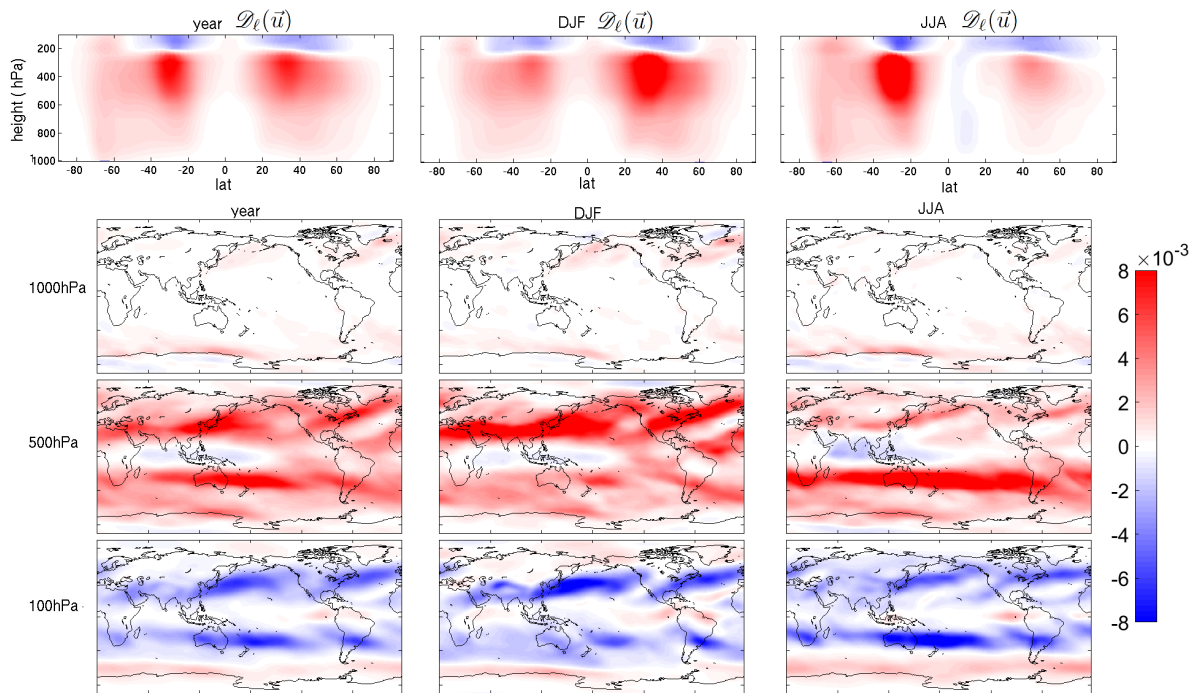
464



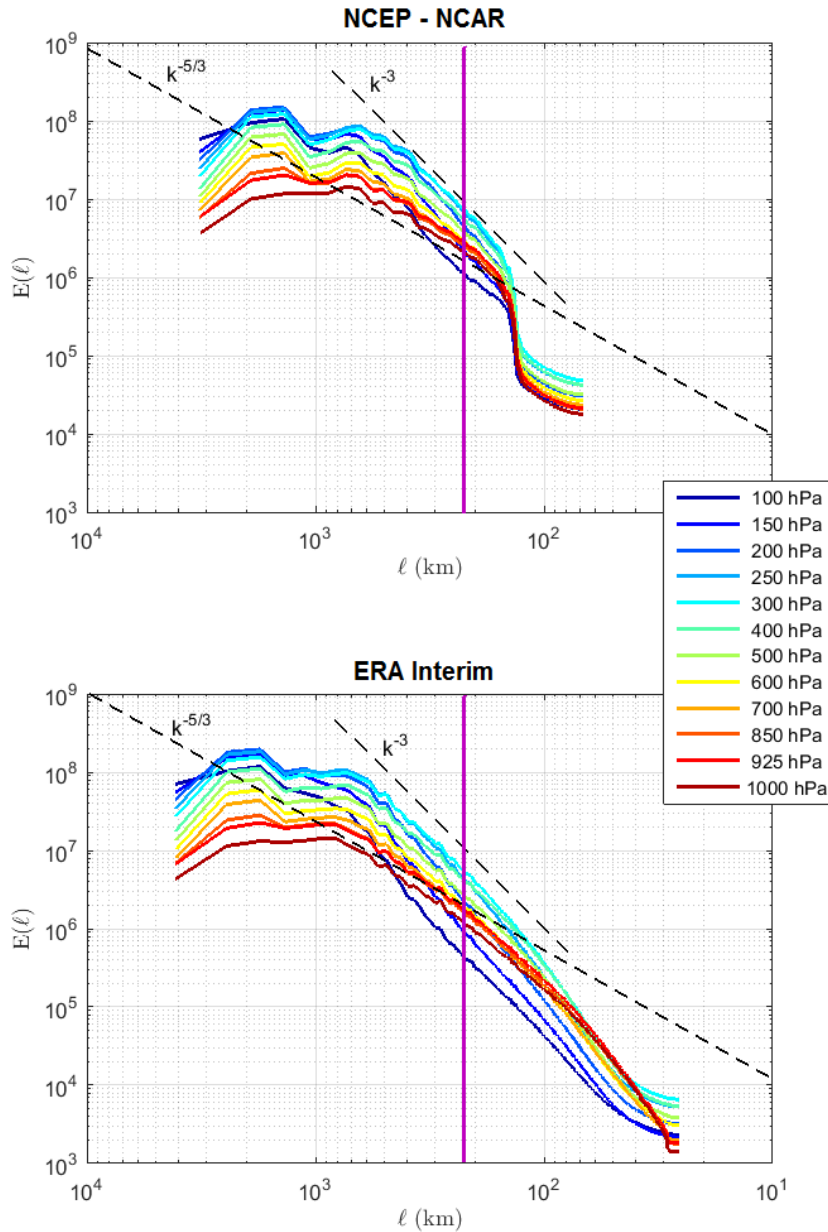
465 FIG. 1. Schematic representation of velocity fields (arrows) possibly originating large positive (orange) or
 466 negative (blue) local energy transfers $\mathcal{D}_\ell(\vec{u})$ (color patches).



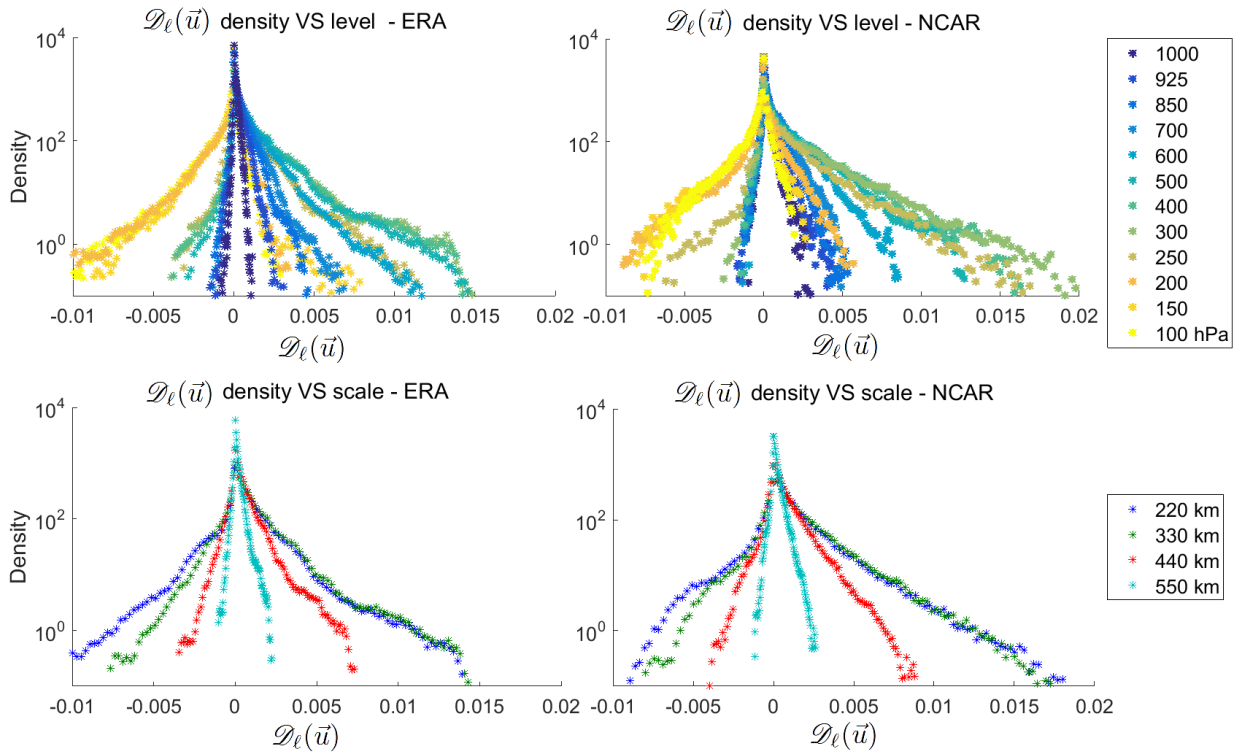
467 FIG. 2. Distribution of $\mathcal{D}_\ell(\bar{u})$ for $\ell = 220$ Km and the ERA-Interim reanalysis. The left panels show the all
 468 2005 year average, the central the winter average, the right panels the summer averages. The maps show the
 469 average $\mathcal{D}_\ell(\bar{u})$ for three different fixed height: 1000 hPa, 500 hPa and 100hPa.



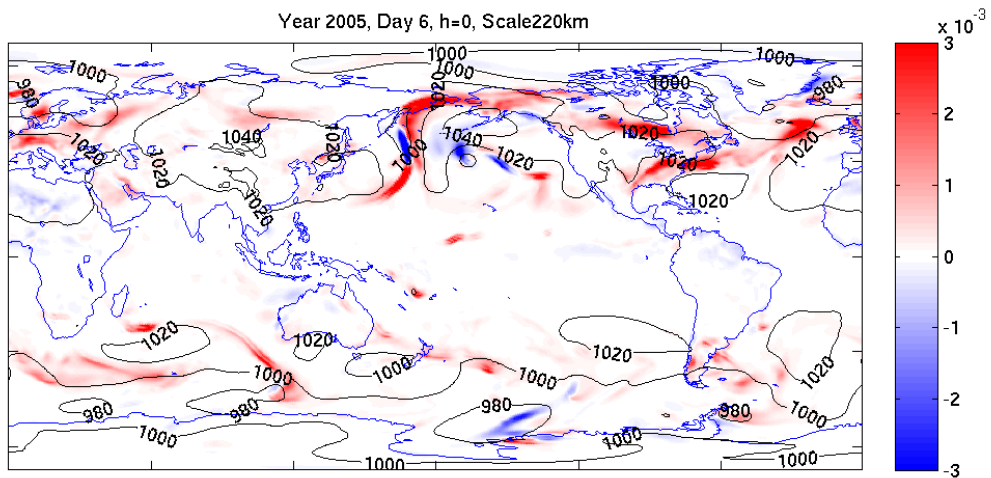
470 FIG. 3. Distribution of $\mathcal{D}_\ell(\bar{u})$ for $\ell = 220$ Km and the NCEP-NCAR reanalysis. The left panels show the all
 471 2005 year average, the central the winter average, the right panels the summer averages. The maps show the
 472 average $\mathcal{D}_\ell(\bar{u})$ for three different fixed height: 1000 hPa, 500 hPa and 100hPa.



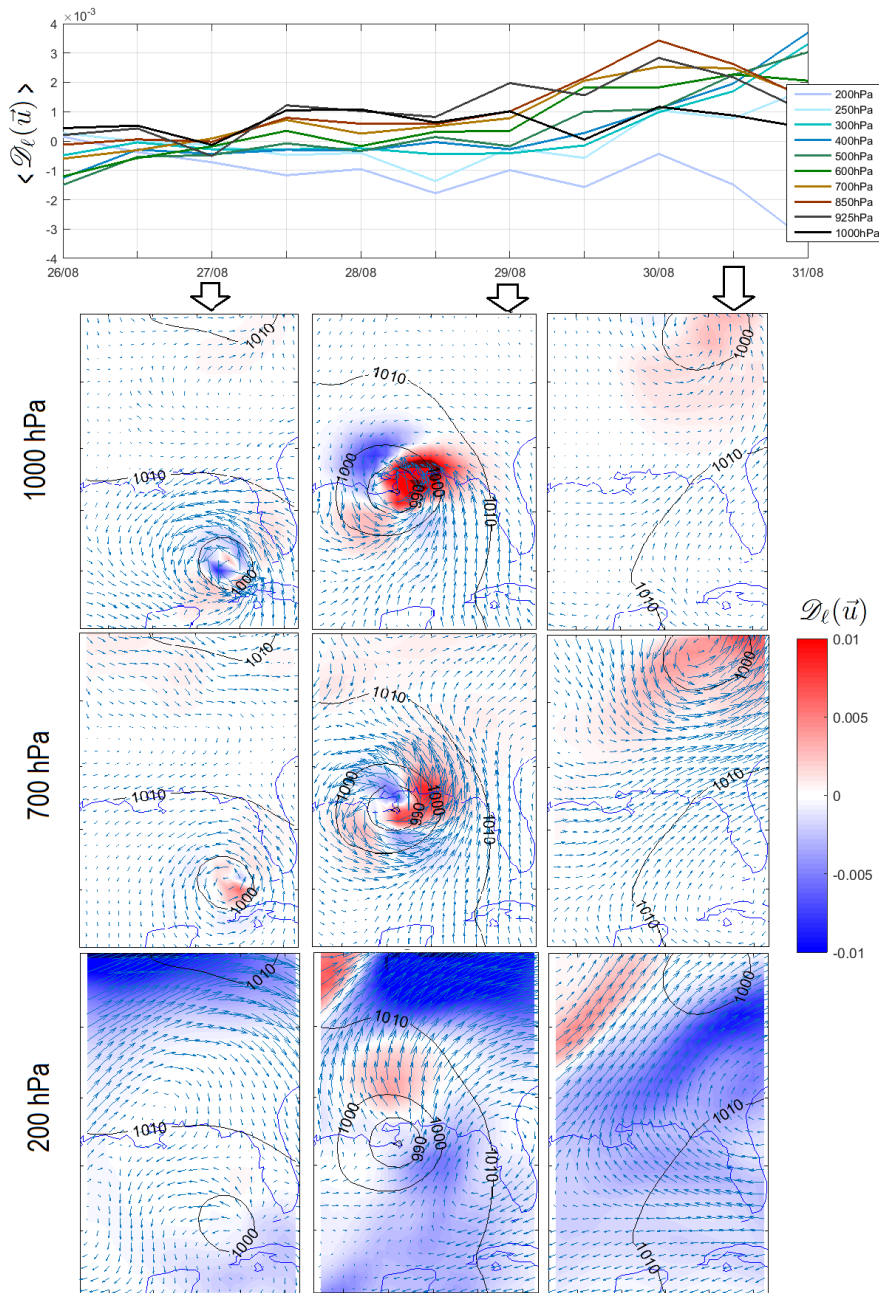
473 FIG. 4. Solid lines: spectra $E(\ell)$ computed, at each pressure level, for the horizontal velocity fields. Dotted
 474 lines: $-5/3$ and -3 slopes. Magenta vertical lines: $\ell = 220$ Km. Top: NCEP-NCAR reanalysis, Bottom: ERA
 475 Interim reanalysis.



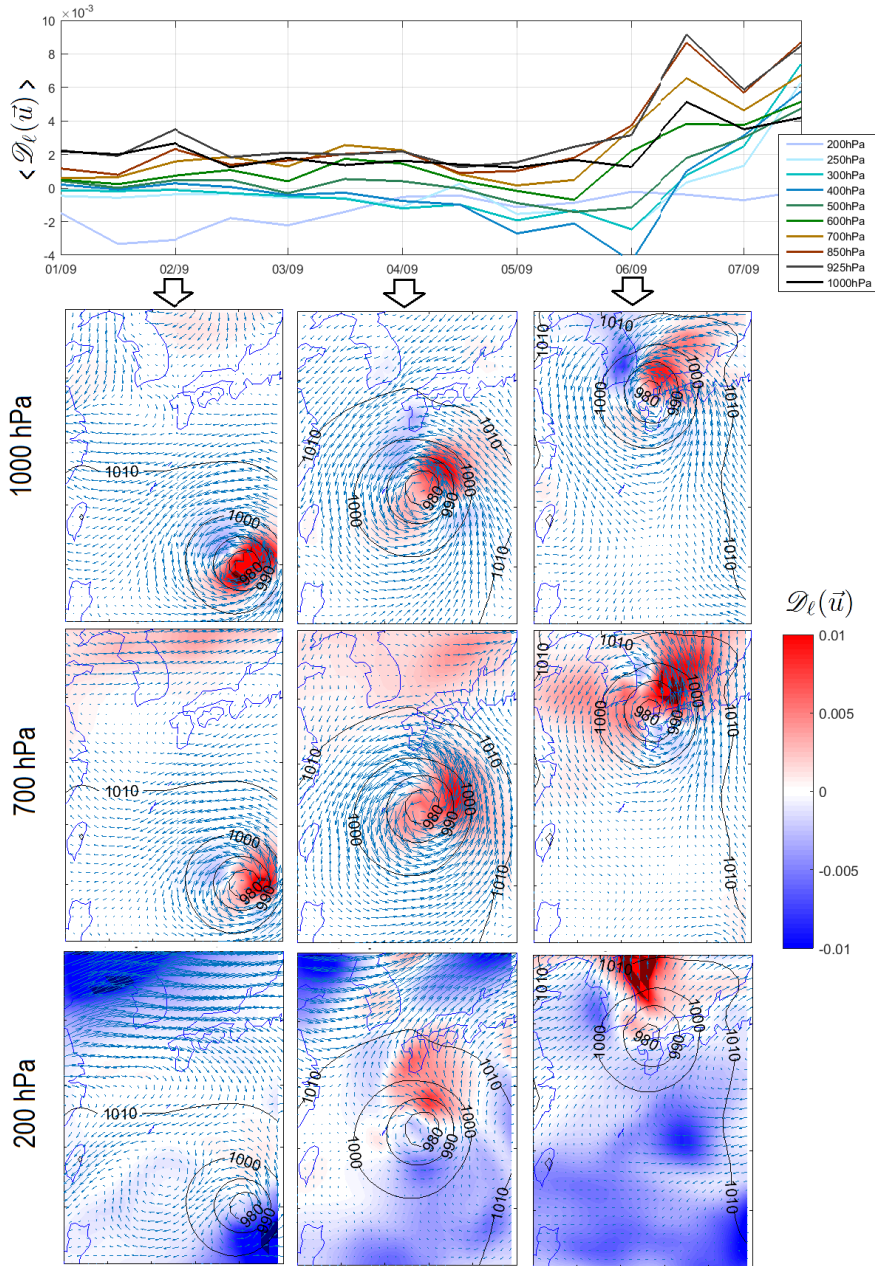
476 FIG. 5. Empirical $\mathcal{D}_\ell(\vec{u})$ density functions for ERA-Interim (left) and NCEP-NCAR (right) and the year 2005.
 477 Upper panel show the dependence on the height for $\ell = 220$ km, lower panel that on the scale.



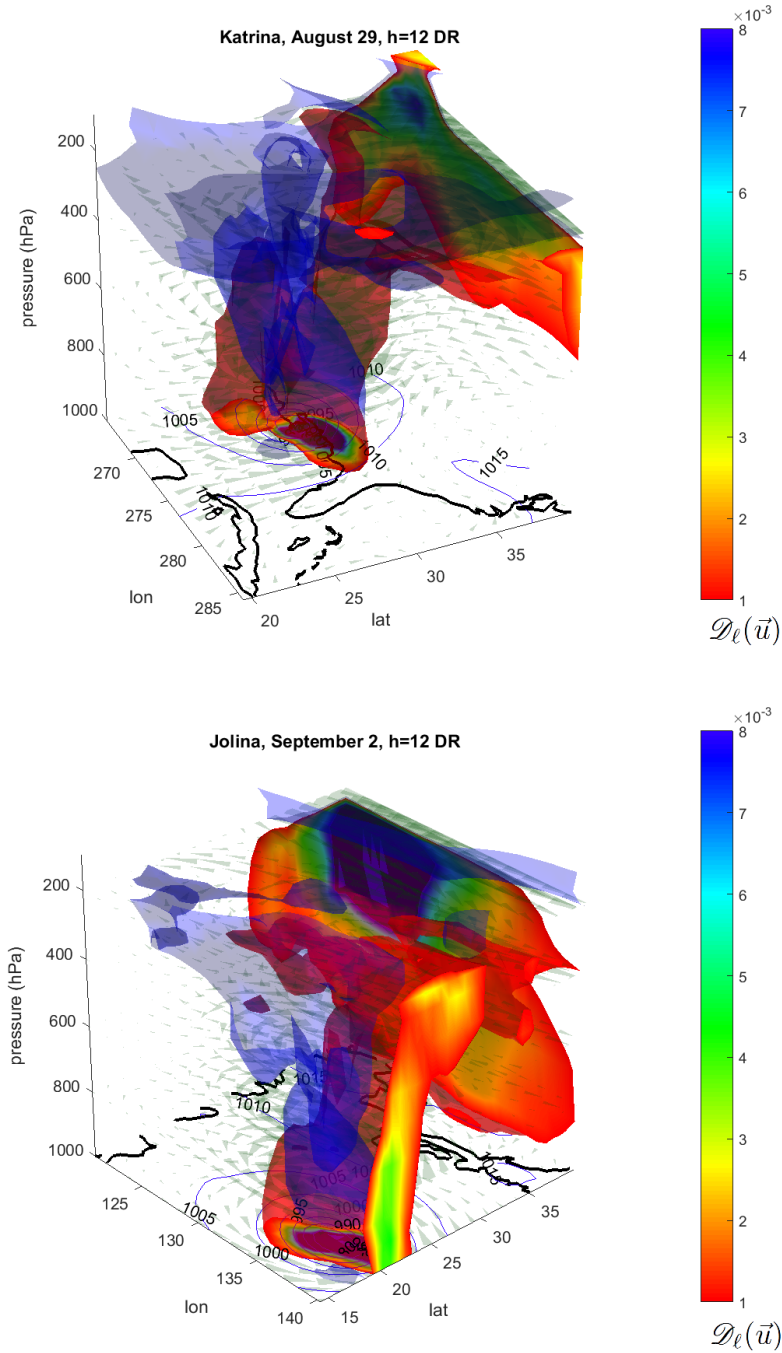
478 FIG. 6. Instantaneous values of $\mathcal{D}_l(\vec{u})$ for ERA-Interim computed for January, 6th at midnight, for $\ell = 220$
 479 km. Black Isolines show the sea level pressure field in hPa.



480 FIG. 7. Katrina Analysis: Spatial average $\langle \mathcal{D}_\ell(\vec{u}) \rangle$ for the region with $p < 1000$ hPa in the regions shown
 481 in the maps, obtained by the ERA-Interim reanalysis, for $\ell = 220$ km. The time interval is 12h and the dates
 482 correspond to midday. The maps show $\mathcal{D}_\ell(\vec{u})$ for three different levels (1000,700 and 200 hPa) at the time
 483 corresponding to the black arrows.



484 FIG. 8. Jolina Analysis: Spatial average $\langle \mathcal{D}_\ell(\vec{u}) \rangle$ for the region with $p < 1005$ hPa in the regions shown in
 485 the maps, obtained by the ERA-Interim reanalysis, for $\ell = 220$ km . The time interval is 12h and the dates
 486 correspond to midday. The maps show $\mathcal{D}_\ell(\vec{u})$ for three different levels (1000,700 and 200 hPa) at the time
 487 corresponding to the black arrows.



488 FIG. 9. 3D structure of the wind field (green cones) and $\mathcal{D}_\ell(\vec{u})$ for the Hurricane Katrina (top) and Jolina
 489 (bottom), obtained by the ERA-Interim reanalysis, for $\ell = 220$ km. Red: isosurfaces at $\mathcal{D}_\ell(\vec{u}) = 0.001$. Dark
 490 Blue: isosurfaces at $\mathcal{D}_\ell(\vec{u}) = -0.001$. The colorscale indicates values $\mathcal{D}_\ell(\vec{u}) > 0.001$. See supplementary videos
 491 for the animations.